High-temperature mechanical behavior of proton-conducting yttrium-doped barium zirconate perovskite

D.Ciria[a,b]**, M. Jiménez-Melendo[b]*, V. Aubin[c], G.Dezanneau[a]

[a] *Laboratoire Structures, Propriétés et Modélisation des Solides, UMR8580, CentraleSupelec, CNRS, Université Paris-Saclay, 3 Rue Joliot-Curie 91190 Gif Sur Yvette, France*

[b] *Laboratoire Mécanique des Sols, Structures et Matériaux, UMR8579, CentraleSupelec, CNRS, Université Paris-Saclay, 3 Rue Joliot-Curie 91190 Gif Sur Yvette, France*

[c] *Departamento de Física de la Materia Condensada, Universidad de Sevilla, Aptdo. 1065, 41080 Sevilla, Spain*

Abstract

Polycrystalline yttrium-doped barium zirconate with composition $BaZr_{0.85}Y_{0.15}O_{2.925}$ has been fabricated from nanopowders synthetized by a modified EDTA-citrate complexing method and conventionally sintered at 1600 °C for 24h. The material exhibits a single cubic perovskite phase, with a homogeneous, dense and fine-grained microstructure consisting of equiaxed grains with an average size of 0.2 μm. Mechanical tests were carried out in compression between 1100 and 1325 °C in air at constant initial strain rate and at constant load. As the temperature increases and/or the strain rate decreases, a gradual transition from brittle-to-ductile behavior was found. In the brittle regime, the fracture is governed by an intergranular failure mode. In the ductile region, grain boundary sliding is the main deformation mechanism, characterized by a stress exponent of 2 and an activation energy of 570 kJ/mol. This is the first report on the creep properties of barium zirconate.

Keywords: Mechanical properties, Creep, Yttrium doped barium zirconate, SOFC electrolyte

* Corresponding author:

Tel: +34 954 550938

E-mail: melendo@us.es

** Corresponding author:

Tel: +34 954 55 64 23

E-mail: dciria@us.es

1 Introduction

Mixed metal oxides of formula ABO_3 (where A and B denote site cations) with perovskite structure are receiving increasing attention due to their outstanding physical and chemical properties for important practical applications in many fields, particularly in electrical insulation (pyro- and ferroelectricity), solar cells, chemical sensors and memory devices, and more recently in the field of electrochemical energetics as electrolytes in solid oxide fuel cells (SOFCs) due to their high proton conductivity at intermediate and elevated temperatures [1-4]. Substitution of B sites by trivalent ions in these perovskite oxides causes the formation of oxygen vacancies, which allow for protonic conduction upon exposure to water vapor at relatively high temperatures. However, practical use of SOFC devices are presently limited by concerns of long-term durability and reliability [5-7]. Physical and chemical alterations, creep deformations and thermo-elastic mismatches between SOFC components induce severe stresses in the system, giving raised to a variety of degradation mechanisms which limit the overall performance of the device [8-11].

Yttrium-doped barium zirconate is a prototype of proton conducting perovskites, exhibiting an elevated electrical conductivity and an excellent chemical stability over a large range of temperatures and oxygen partial pressures [3, 12, 13]. Numerous studies have investigated their processing, structure and electro-chemical characteristics [3, 14-18]. However, the high-temperature mechanical response of these protonic conducting materials has not been reported yet, despite the utility of such investigations for predicting the mechanical degradation and performance of these device components. Furthermore, high-temperature plastic deformation studies provide valuable information about mass transport-controlled processes, such as sintering, densification and grain growth, which are essential to devise optimum processing schedules.

The objective of this work is therefore to study their mechanical behavior of 15 at% yttrium-doped barium zirconate policrystals at elevated temperatures. Compressive deformation tests were carried out at constant cross-head speed and at constant load in the temperature range between 1100 and 1325 °C in air. Mechanical data have being correlated with microstructural observations in order to identify the underlying microscopic mechanisms responsible for the plastic deformation.

2 Experimental details

2.1 Sample preparation

Dense 15 at% Y-doped barium zirconate $BaZr_{0.85}Y_{0.15}O_{2.925}$ (BZY) polycrystals have been fabricated by a conventional ceramic route starting from nanopowders synthesized by a combined ethylene-diamine-tetraacid (EDTA)/citrate complexing method [19]. High purity (> 99.5%) commercial powders of $Ba(NO_3)_2$ (Alfa-Aesar), $Y(NO_3)_3 \cdot 6H_2O$ (Alfa-Aesar) and $ZrO(NOx) \cdot yH_2O$ (Strem Chemicals) were used as starting precursors. Proper amounts of nitrates were dissolved in ultra-pure water, followed by the addition of citric acid and EDTA as chelating agents; aqueous ammonia was also added to facilitate EDTA dissolution. The reaction solution was heated at 100 °C under continuous stirring to obtain a viscous gel, which was submitted to microwave-assisted

combustion for 2 h, resulting a blackish porous precursor. This precursor was then calcined at 1000 °C for 5 h in air to obtain a single crystalline phase powder (as checked by X-ray diffraction, see below), which was uniaxially pressed at 100 MPa and then isostatically pressed at 750 MPa for 10 min. These green compacts were finally sintered at 1600 °C for 24 h in air. To prevent barium evaporation during sintering, the pellets were buried into a powder mixture of the fabricated BZY powder with a 10 wt%-excess barium carbonate [14]. Bulk densities of 5990 ± 20 kg/m^3 were determined by weight/dimensions measurements, corresponding to a relative density of 97.1 ± 0.3 %; a theoretical value of 6166 kg/m^3 has been used for 15 at% yttrium-doped barium zirconate, assuming a lattice parameter of a = 4.223 Å for this composition (as experimentally found, see below).

2.2 Structural and microstructural characterization

The structural analysis of the crystalline phases in both the calcined powders and sintered polycrystals was performed by using a Brucker AXS Advance D2 diffractometer (X-Ray Laboratory, SPMS, Centrale Supelec, France) in Bragg-Brentano configuration with Cu-Kα radiation (λ = 1.54060 Å) filtered with nickel. Data were collected in the 2θ region between 20° and 130° with a step size of 0.02° and 10 s/step of acquisition. X-ray spectra were processed by the Le Bail refinement method using the EVA2 Brucker AXS software package and the reference pattern 04-015-2511 (PDF-2002 ICDD database) corresponding to $BaZr_{0.8}Y_{0.2}O_{3-\delta}$ (a = 4.22 Å, cubic $Pm\bar{3}m$).

The microstructural characterization of as-prepared and deformed polycrystals was performed using a high-resolution FEI Teneo scanning electron microscope (HRSEM) (Microscopy Service, CITIUS, University of Sevilla, Spain). To reveal grain boundaries, longitudinal sections were cut from the samples, mechanically polished and then thermally etched at 1300 °C for 3 hours in air. The most relevant morphological parameters, the grain size d (taken as the equivalent planar diameter) =4(grain area)/$\pi^{1/2}$, form factor F = 4π (grain area)/(grain perimeter)^2 and orientation angle θ of the largest grain diameter were measured from SEM micrographs using a semiautomatic image analyzer averaging over more than 500 grains. Fracture surfaces of strained samples that either failed during testing or were intentionally broken at room temperature were also characterized by HRSEM. The internal structure of the grains was examined in a FEI Talos transmission electron microscope (TEM) operating at 200 kV voltage (Microscopy Service, CITIUS, University of Sevilla, Spain). To this end, slices were cut from as-fabricated and deformed samples and thinned to electron transparency by conventional mechanical polishing, dimpling and ion-milling.

2.3 Mechanical characterization

Parallelepipedic specimens of 5 x 3 x 3 mm in size were cut from the sintered pellets and used for mechanical testing. Compression tests were carried out in air at temperatures T between 1100 and 1325 ˚C (0.50 - 0.60 T_m, where T_m = 2775 K is the melting temperature of $BaZrO_3$) in a universal testing machine at constant cross-head speeds between 5 and 50 μm/min, corresponding to initial strain rates $\dot{\varepsilon}_o$ between 1.8x10^{-5} and

$1.8x10^{-4}$ s^{-1}. Compressive tests were also conducted at constant load at nominal stresses between 50 and 100 MPa in the same temperature range. The specimens were sandwiched between CSi pads in order to reduce the friction with the alumina punching rods of the deformation machine, which tends to cause plastic constrictions at the ends of the specimen. The data recorded at constant cross-head speed, load vs. time, were plotted as σ-ε curves, where ε is the true strain ($\varepsilon = \ln(l_o/l)$, with l_o and l the initial and instantaneous length, respectively) and σ is the true stress ($\sigma = \sigma_o.e^{(-\varepsilon)}$, with σ_o the initial stress). Data recorded at constant load, specimen height vs. time, were plotted as $\log \dot{\varepsilon}_o - \varepsilon$ curves, where $\dot{\varepsilon}$ is the instantaneous strain rate.

The mechanical data were analyzed using the standard high-temperature power law for steady-state deformation [20]

$$\dot{\varepsilon} = A\sigma^n d^{-p} \exp\left(-\frac{Q}{RT}\right) \quad (1)$$

where A is a parameter depending on the deformation mechanism, d is the grain size, n is the stress exponent, p is the grain size exponent, Q is the activation energy for creep and R is the gas constant. Two independent testing procedures were used to evaluate the creep parameters n and Q: the conventional method, in which different samples are submitted to identical experimental conditions but changing just one variable (strain rate, temperature or load) at a time; and the differential method, where a single specimen is submitted to up and down changes of one variable, keeping constant the others.

3 Results and discussion

3.1 Crystal structure

Fig. 1 shows the X-Ray diffraction (XRD) patterns of the calcined powders and sintered pellets of BZY, confirming the presence of the single perovskite phase with space group $Pm\bar{3}m$ in both cases. XRD patterns were fitted by the Le Bail method, resulting in a refined lattice parameter of a = 4.203(1) Å for the nanometric powder, in agreement with values previously reported for BZY with the same composition powders [21, 22]. The crystallite size, estimated from diffraction peak width by using the Scherrer law, was 15-20 nm. A slightly larger lattice parameter a = 4.223(2) Å was found in the sintered material. Duval *et al.* [22] also reported such an increase in lattice constant in BZY, which was associated with the incompleteness of the precursor-reaction formation at temperatures below 1250 °C [23] (the calcination temperature in the present work was 1000 °C).

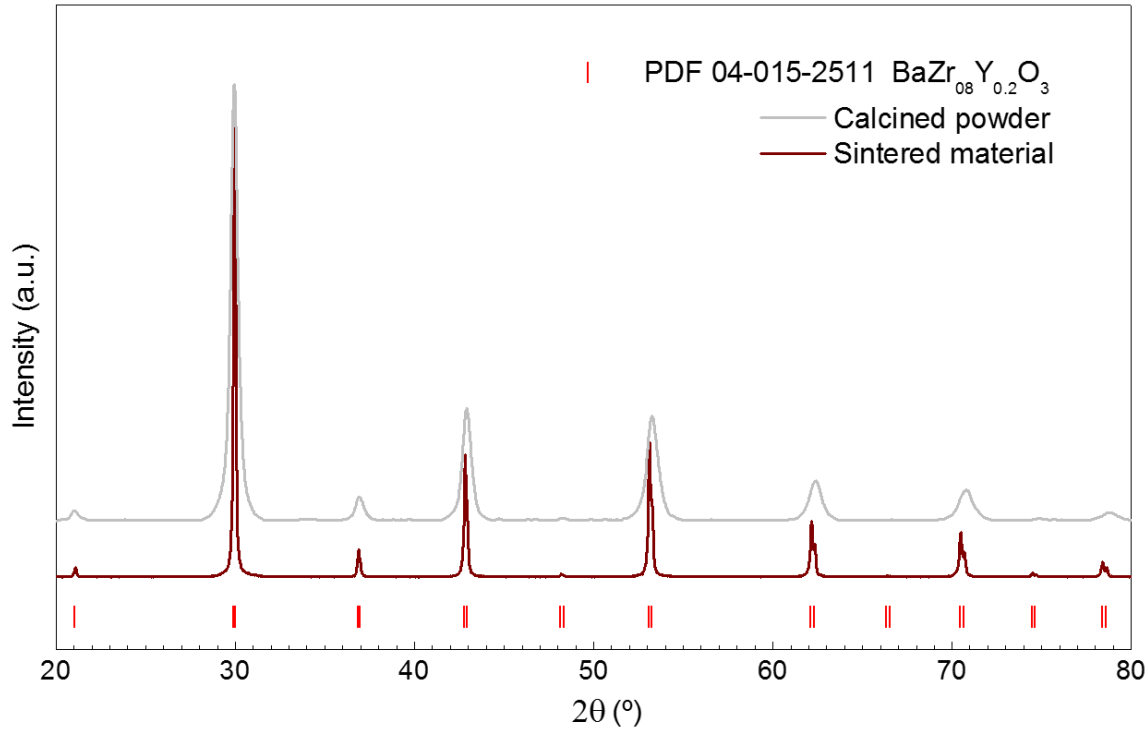

Fig. 1. X-ray diffraction patterns of calcined powders and sintered pellets of $BaZr_{0.85}Y_{0.15}O_{2.925}$. PDF-2002 pattern for $BaZr_{0.8}Y_{0.2}O_3$ is also shown.

3.2 Microstructure of sintered BZY

Fig. 2 shows SEM micrographs of polished and thermally etched BZY cross-sections revealing the microstructure of the material. Porosity is small, according to density measurements, consisting in pores below 100 nm in size located at multiple grain junctions. The grains exhibit an equiaxed shape without preferential orientation, with a mean form factor F = 0.79 ± 0.09 (**Fig. 3**a). The grain size distribution follows a log-normal law (**Fig. 3**b), as usually found in ceramics, with an average grain size of 0.20 ± 0.10 µm.

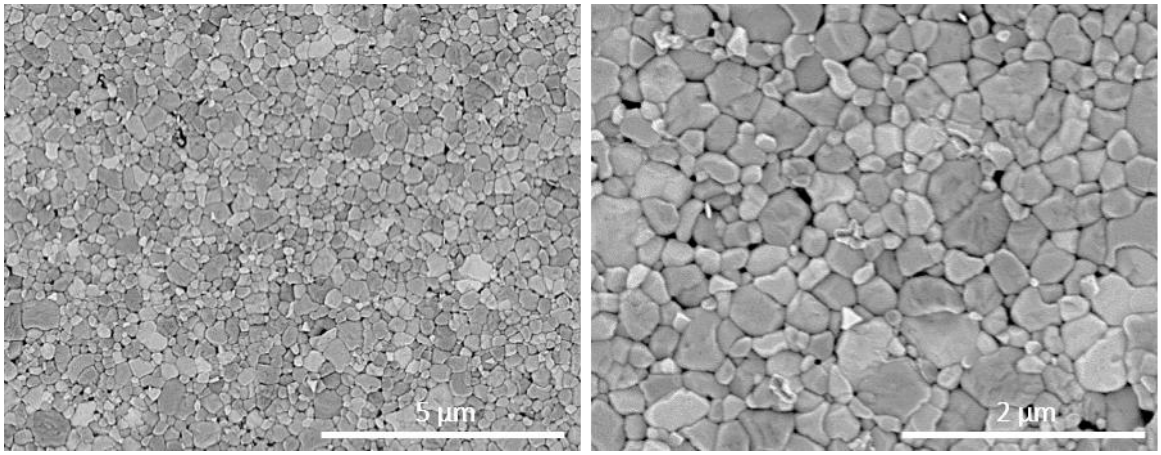

Fig. 2. SEM micrographs of sintered BZY.

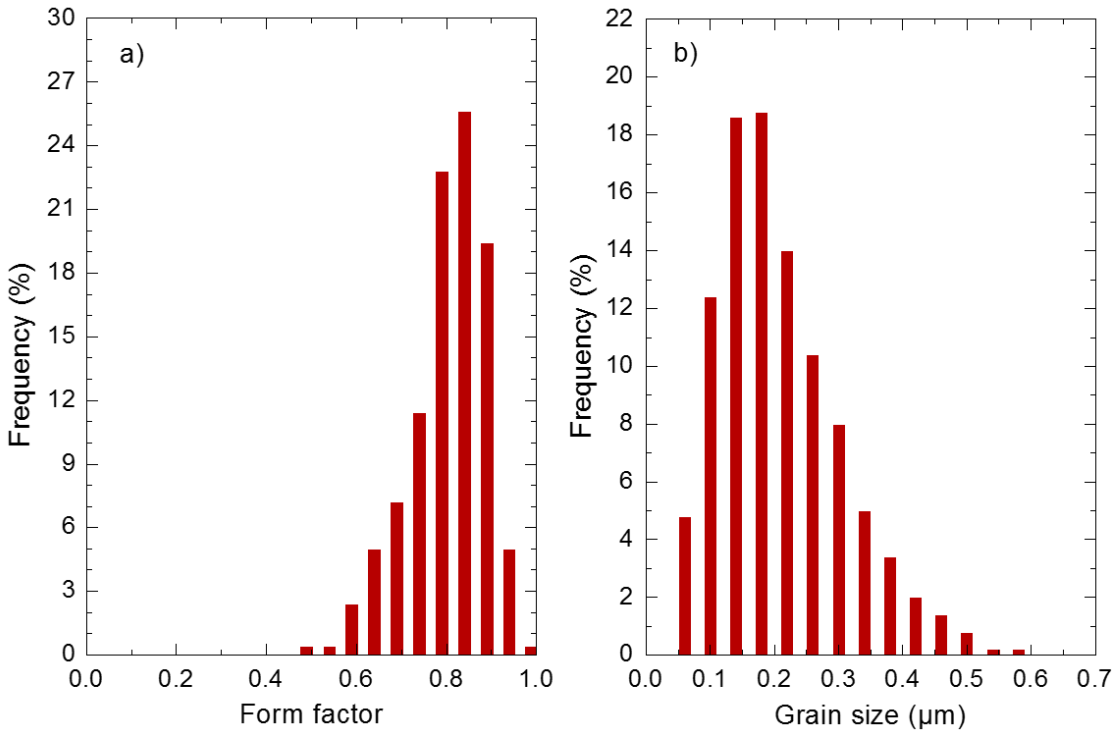

Fig. 3. Morphological distributions of $BaZr_{0.85}Y_{0.15}O_{2.925}$. (a) Form factor; (b) Grain size.

Fig. 4 shows representative TEM micrographs of as-sintered BZY. Grains are well faceted and equiaxed, without secondary phases along grain boundaries and triple grain junctions. Grains are often stressed, particularly the larger ones, showing a high density of dislocations arranged in tangles and also forming pile-ups and low-angle sub-boundaries. Such dislocation configurations indicate that grain boundaries are not efficient sites for dislocation absorption, allowing a considerable strain energy to be accumulated by the grain structure. This feature may be at the origin of the poor sinterability of this compound.

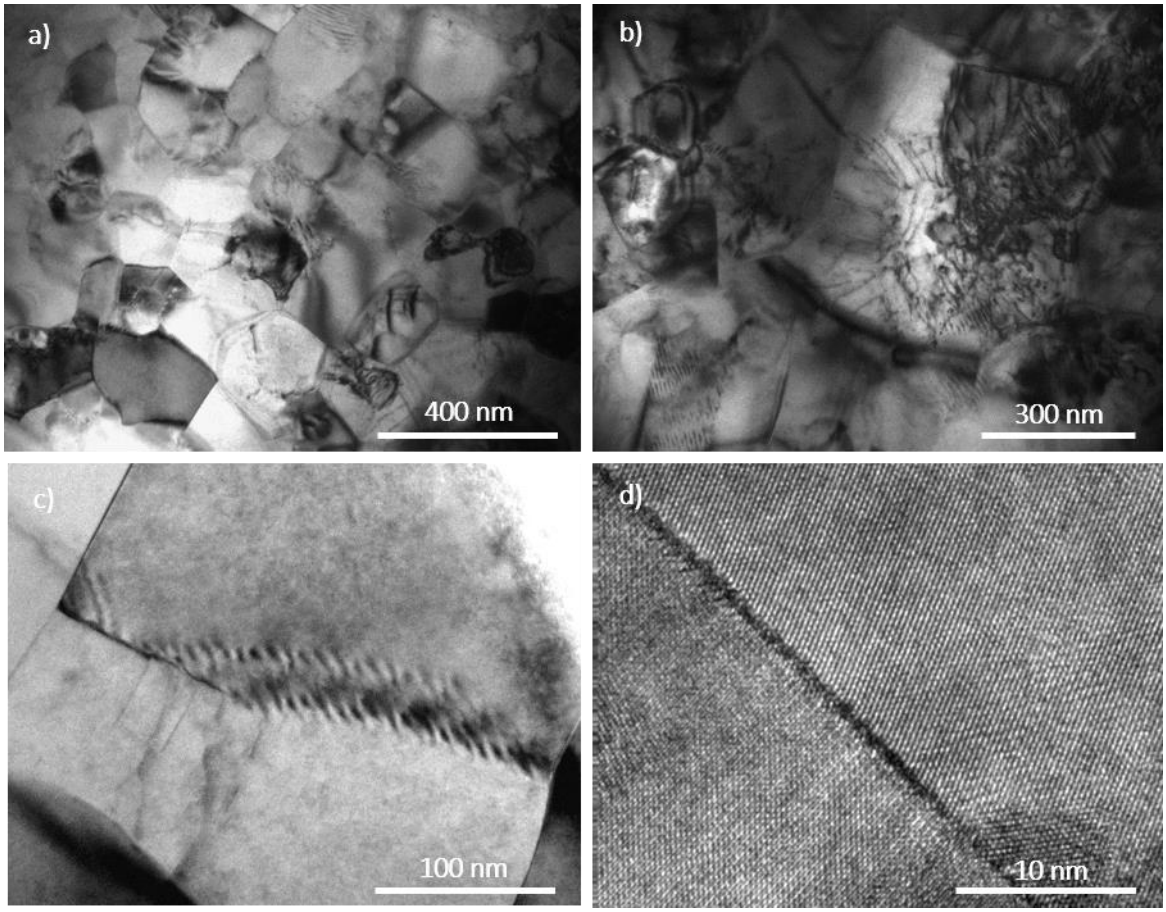

Fig. 4. TEM images of as-sintered BZY showing: (a) the overall grain structure, (b) and (c) different dislocation arrangements in the larger-sized grains, and (d) the absence of secondary phases along grain boundaries.

3.3 High-temperature mechanical behavior

The variation of true stress σ with true strain ε for different deformation conditions of temperature T and initial strain rate $\dot{\varepsilon}_o$ are shown in **Fig. 5**. The material displays a gradual transition from a brittle-to-ductile regime as the temperature increases and/or the strain rate decreases. At 1100 °C, the lowest temperature studied, the sample failed catastrophically without undergoing any plastic deformation at a stress level of 825 MPa (curve in yellow, **Fig. 5**a). A semi-brittle behavior was observed at 1175 and 1210 °C, where the samples underwent a relatively large plastic deformation of 15 – 25% before catastrophic failure. At higher temperatures (**Fig. 5**a) and/or lower strain rates (**Fig. 5**b), the material displays extended steady states of deformation characterized by a positive and rather constant slope of the σ - ε curves; such a slope gradually decreases with increasing temperature or decreasing initial strain rate, as expected in compressive constant cross-head speed tests. Test were intentionally stopped at ε = 40% for subsequent microstructural observations.

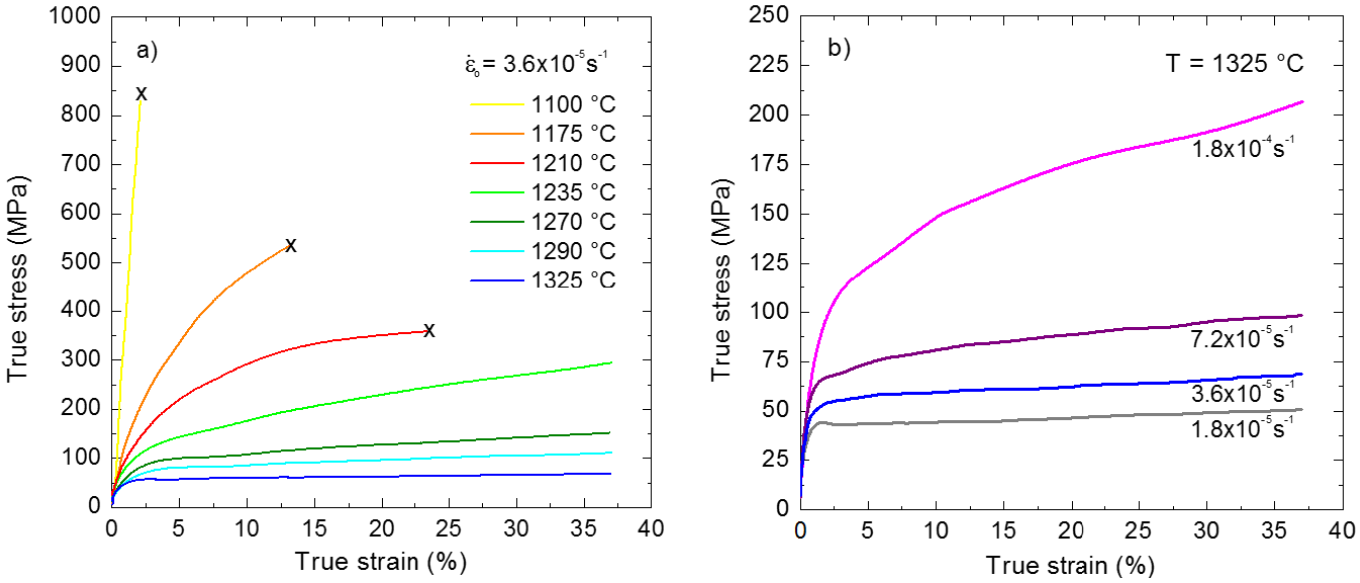

Fig. 5. True stress σ- true strain ε curves for BZY deformed: (a) at an initial strain rate of 3.6x10^{-5} s^{-1} as function of temperature; and (b) at 1325 °C as function of initial strain rate. Marks "x" indicate macroscopic specimen failure.

The macroscopic aspect of the samples after deformation (**Fig. 6**) agrees well with the shape of the corresponding mechanical σ - ε curves. At 1100 °C, the sample completely fractured into multiple small fragments, indicating the fast propagation of cracks throughout the entire volume of the samples. SEM observations of these fracture surfaces indicate an intergranular failure mode (**Fig. 7**a), as could be expected in a such very fine-grained material. At 1175 and 1210 °C, in the semi-ductile regime (curves in orange and red in **Fig. 5**a), the specimens underwent a strain-controlled delayed fracture, originated by damage accumulation. To determine the origin of this damage-tolerant regime, the test performed at 1175 °C (curve in orange, **Fig. 5**a) was repeated but voluntarily stopped at a strain of 10%, prior to failure. SEM observations of cross-sections parallel to the loading axis of this specimen (**Fig. 7**b) show a high density of microcavities along grain boundaries distributed throughout the sample; as strain proceeds, these stress-assisted microcavities coalesce into cracks leading to the final sample failure. These observations agree with the intergranular fracture mode noted above.

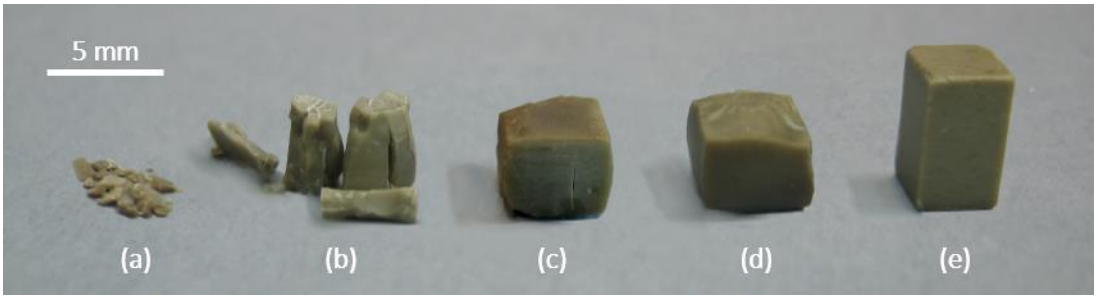

Fig. 6. Macroscopic aspect of BZY samples deformed in compression at an initial strain rate of 3.6x10^{-5} s^{-1} and different temperatures: (a) 1100 °C, (b) 1175 °C, (c) 1235 °C, (d) 1290 °C and (e) as-prepared.

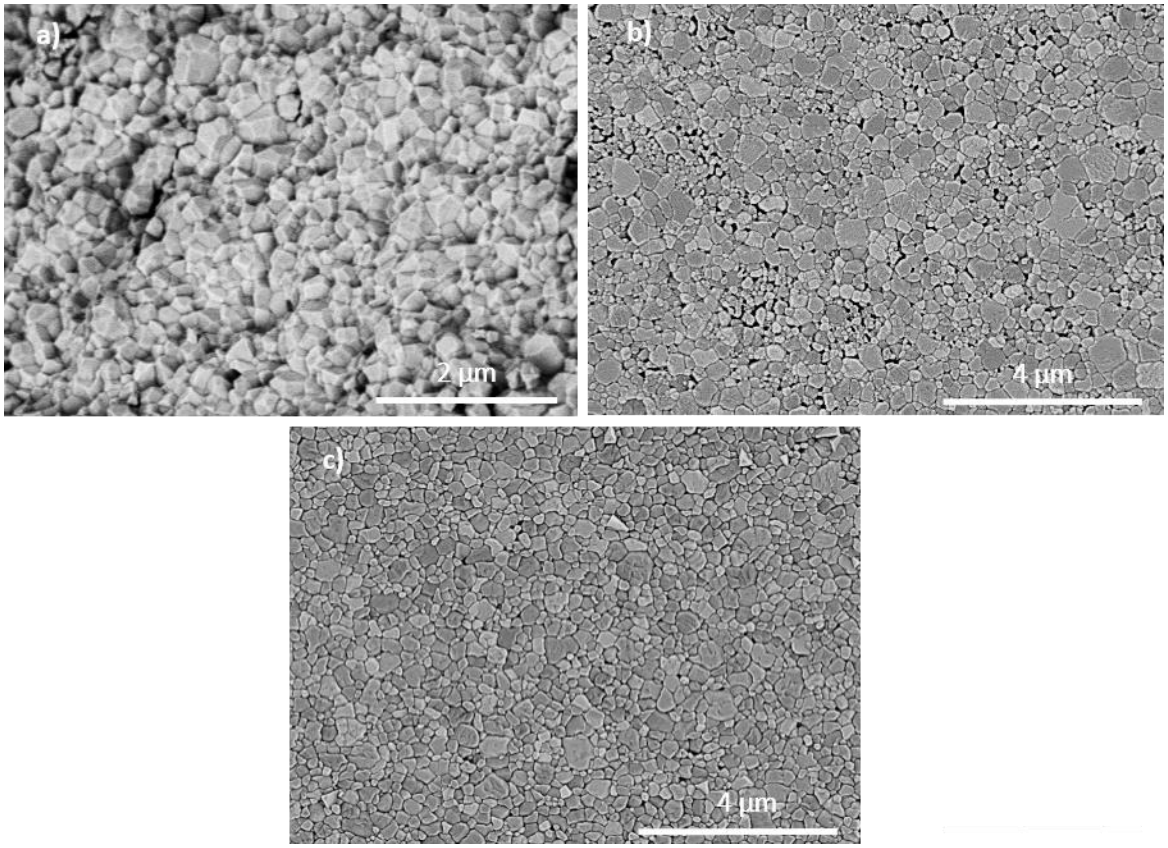

Fig. 7. SEM micrographs of BZY samples deformed at different conditions: (a) fracture surface at 1100 °C and $3.6x10^{-5}$ s^{-1}; (b) deformed up to ε = 10% at $3.6x10^{-5}$ s^{-1} and 1175 °C (semi-brittle regime); and (c) deformed up to ε = 40% at $3.6x10^{-5}$ s^{-1} and 1235 °C (ductile regime). Note the different microcavitation between samples (b) and (c). Stress axis is vertical.

At temperatures of 1235 °C and above, the samples deformed homogeneously with very little barreling (**Fig. 6**c and d), in agreement with the well-established steady states of deformation. SEM observations of samples deformed in these steady-state conditions (**Fig. 7**c) show the lack of noticeable changes in grain morphology and porosity with respect to as-fabricated samples. No concurrent grain growth was found even at the highest temperature and lowest strain rate studied (1325 °C and $1.8x10^{-5}$ s^{-1}, respectively, curve in grey in **Fig. 5**b): the corresponding grain size d and form factor F distributions measured at these conditions led to average values of d = 0.19 ± 0.08 µm and F = 0.80 ± 0.09, identical to those found in unstrained samples (d = 0.20 ± 0.10 µm and F = 0.79 ± 0.09). The lack of morphological changes during deformation suggests that grain boundary sliding is the dominant mechanism for steady deformation in this material, as found in other fine-grained ceramics [24-31].

TEM observations performed on 40%-deformed samples in steady-state conditions (**Fig. 8**) showed that the grains remained equiaxed, without signs of cavitation along boundaries. The overall structure and density of dislocations are similar to those observed in unstrained specimens (**Fig. 4**), suggesting that dislocations do not play an important role in the steady-state deformation of BZY, the grains moving on each other as rigid bodies.

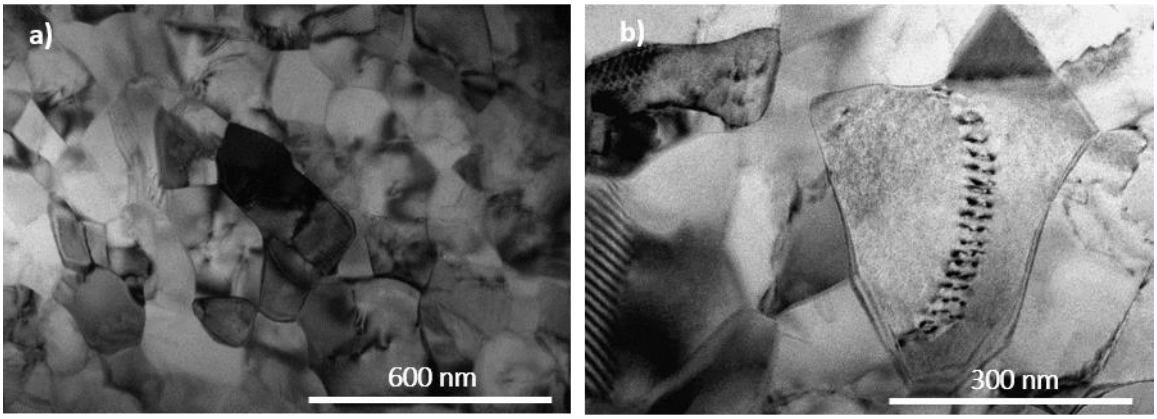

Fig. 8. TEM images of BZY deformed up to 40% at an initial strain rate of 3.6×10^{-5} s^{-1} and 1325 °C showing (a) the grain structure and (b) a dislocation pile-up inside a grain.

3.4 Creep parameters

The stress exponent n in steady-state conditions (Eq. 1) was estimated by different methods. Firstly, it was measured from isothermal σ - ε curves obtained at different initial strain rates (conventional method, **Fig. 9**). The stress exponent was measured at three different strain levels of 10, 20 and 30%, resulting values of n = 2.2, 2.1 and 2.1, with an average value of n = 2.1 ± 0.1. The maintenance of the stress exponent value with strain indicates that no significant microstructural evolution took place during testing, in agreement with the morphological measurements noted above. For the sake of comparison, the creep behavior of 3 mol% yttria-stabilized tetragonal zirconia 3YTZP (the most studied superplastic ceramic) with a grain size of 0.5 μm is also shown in **Fig. 9**. It can be seen that the creep resistance of BZY is much higher than that of 3YTZP, even if the difference in grain size is not taken into account.

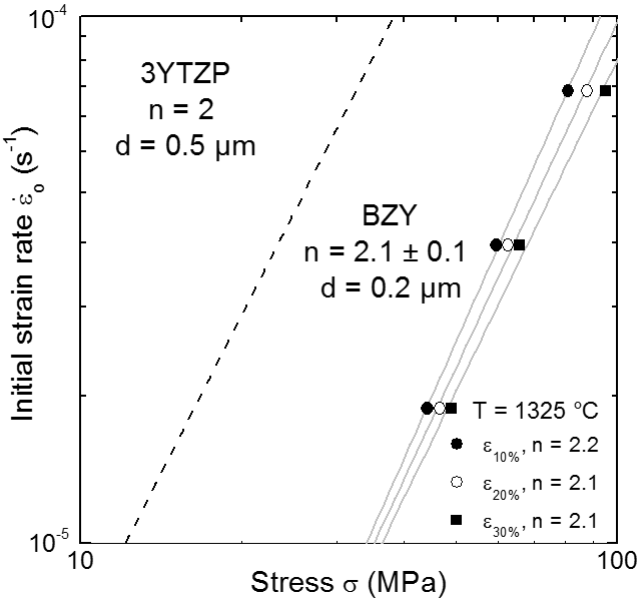

Fig. 9. Variation of strain rate vs stress for BZY at strain levels ε of 10, 20 and 30%. Data for fine-grained (d = 0.5 μm) 3YTZP with n = 2, the reference material for superplasic ceramics, is also shown (dashed line) [25].

The stress exponent was also estimated from fast strain rate changes during isothermal tests (differential method), as illustrated in **Fig.10** for BZY deformed at 1290 °C, which shows several jumps between 3.6×10^{-5} and 1.8×10^{-5} s^{-1}. The comparison of the steady-state flow stresses before and after the changes yields an average exponent of n = 2.1 ± 0.1, in excellent agreement with the value found by the conventional method.

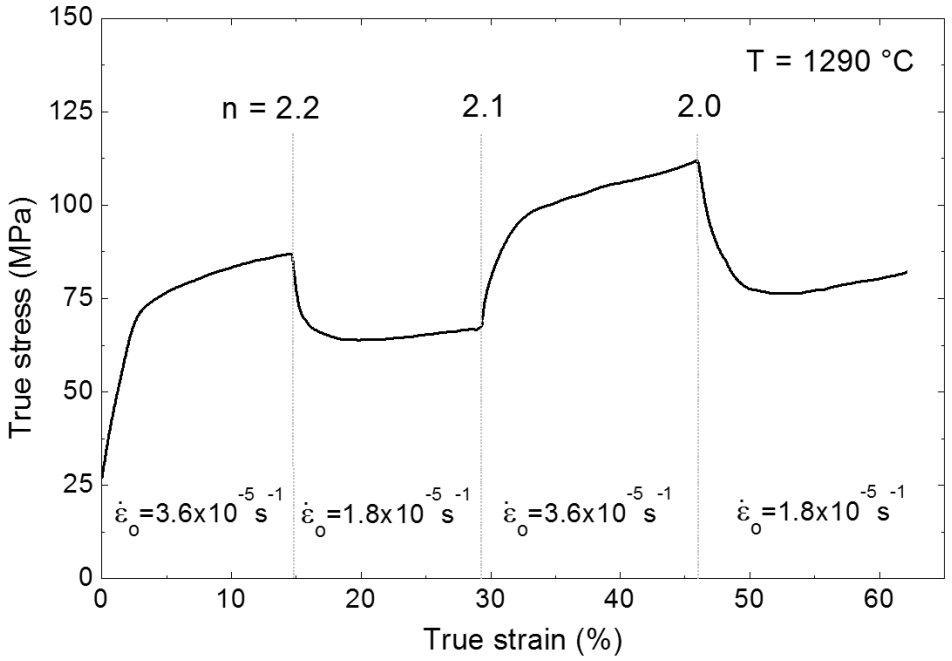

Fig. 10. True stress σ - true strain ε curve for BZY deformed at 1290 °C showing several determinations of n by strain rate changes.

The creep activation energy Q (**Eq. 1**) was also measured by the two methods. Firstly, Q was obtained directly from the iso-strain rate curves obtained at different temperatures in steady state (conventional method, **Fig. 5**a), resulting an average value of Q = 560 ± 40 kJ/mol. The same value of Q = 580 ± 50 kJ/mol was measured from up- and down-temperature changes performed during single iso-strain rate tests (differential method), as shown **Fig. 11** where two determinations of Q by temperature changes are displayed (curve in black). **Fig. 11** also displays the corresponding isothermal tests (curves in green and light blue) superimposed to the differential curve. As can be seen, the curves overlap fairly well at the same experimental conditions, indicating an excellent reproducibility of the high-temperature mechanical tests.

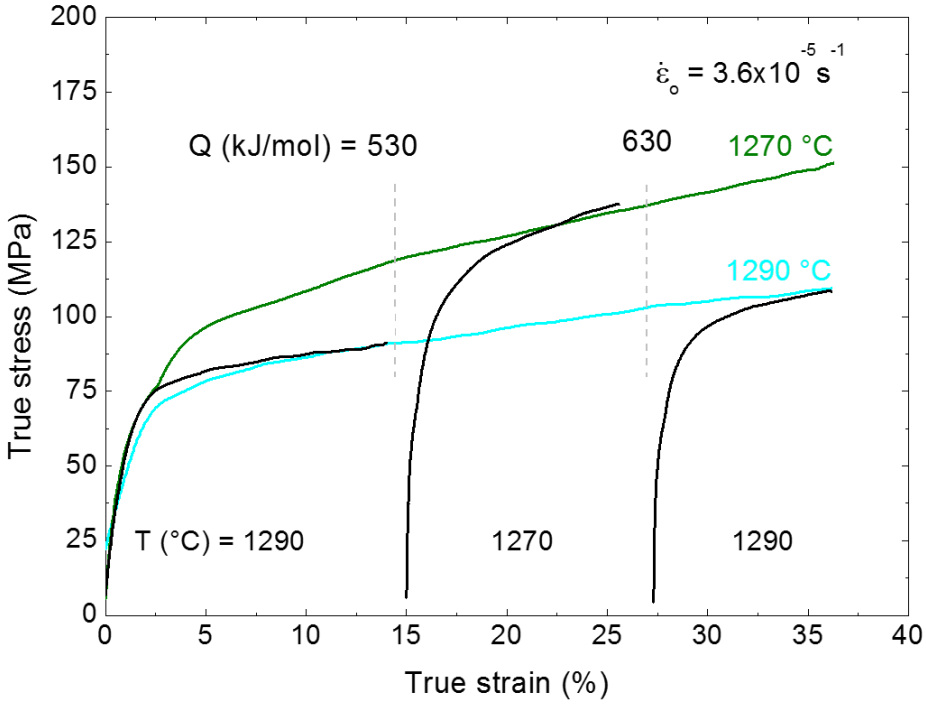

Fig. 11. True stress σ - true strain ε curve for BZY deformed at an initial strain rate of 3.6×10^{-5} s^{-1} showing two determinations of Q by temperature changes between 1270 and 1290 °C (in black). The corresponding isothermal curves are also displayed (in green and light blue, respectively), which overlap well with the differential curve.

In addition to constant strain rate tests, the creep parameters n and Q were also determined from tests performed at constant load. **Fig. 12** displays the log $\dot{\varepsilon}$ - ε curve obtained at 1280 °C showing several determinations of n by fast load changes. Stress exponents of 1.9, 2.0 and 1.9 were estimated, in excellent agreement with the values measured from constant strain rate tests. Two additional features should be noted from this figure: (i) the strain rates after up- and down-load changes remain rather constant, indicating the absence of significant microstructural evolution during creep, in agreement with microstructural observations; and (ii) the steady-state stages are reached immediately upon load changes, which is characteristic of a creep diffusion mechanism, contrary to what is expected for a dislocation-driven mechanism, where a dislocation substructure must be established prior to the attainment of the steady state.

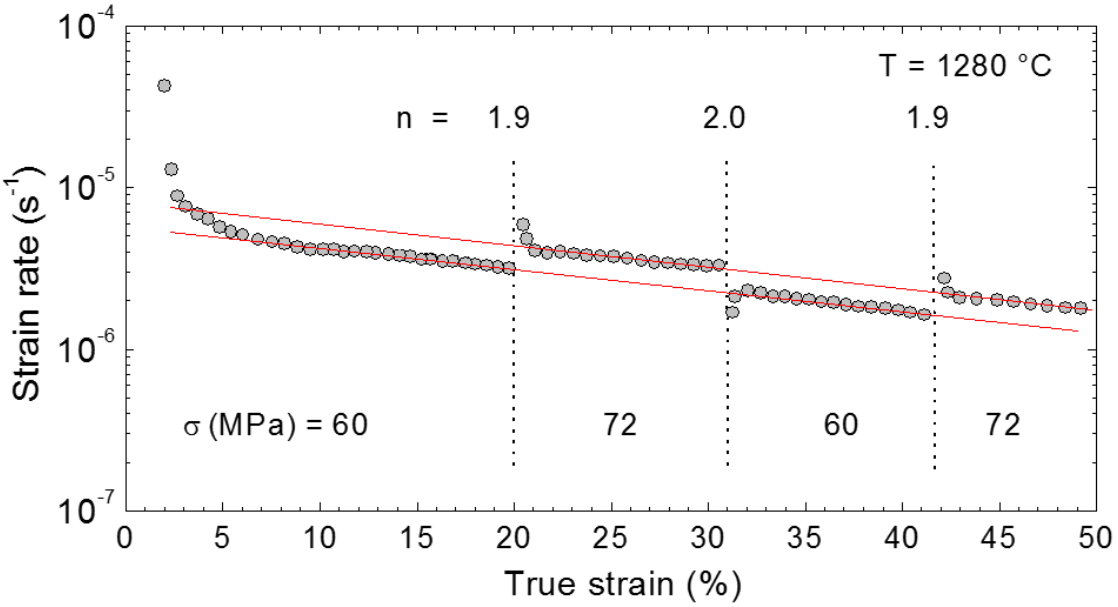

Fig. 12. Creep curve plotted as log $\dot{\varepsilon}$ against ε for BZY deformed at 1280 °C. Several determinations of *n* by load changes are shown. Note the absence of creep transients after changes.

In a similar way, the creep activation energy Q was also measured from temperature changes during constant load tests, as illustrated in **Fig. 13**, where two determinations of Q between 1280 and 1250 °C at σ = 65 MPa are shown. An average value of Q = 560 ± 40 kJ/mol was found, in good agreement with the value deduced from constant cross-head speed tests.

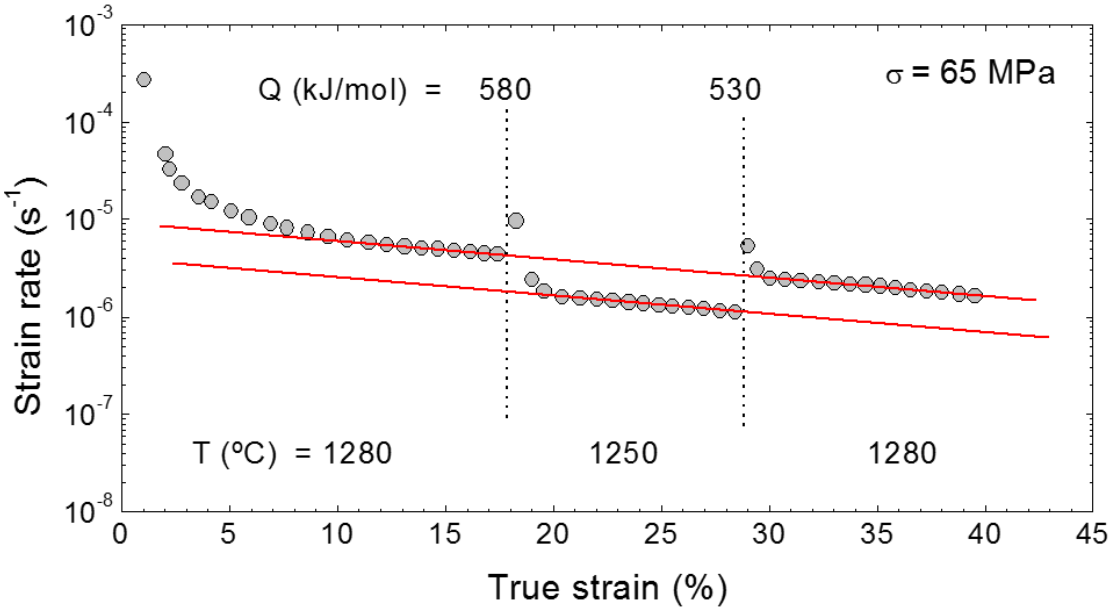

Fig. 13. Creep curve for BZY deformed at 65 MPa showing two determinations of Q by temperature changes.

3.5 High temperature deformation mechanism

The previous results show that the steady-state creep of fine-grained BZY with d = 0.2 µm can be confidently characterized by a stress exponent of 2.0 ± 0.1 and an activation energy of 570 ± 40 kJ/mol. This value of n,

along with the absence of morphological modifications of the grains with strain and the lack of creep transients after stress or temperature changes, strongly suggest that grain boundary sliding is the primary deformation mechanism, with the grains sliding on each other to accommodate the macroscopic deformation of the specimen. Such a mechanism has been widely reported in the creep of fine-grained ceramics with grain sizes below 1 µm, such as alumina [27, 28], barium cerate [29], lanthanum silicate [30] and particularly, 3 mo% yttria-stabilized tetragonal zirconia (3YTZP)[25, 31], the first ceramic material where such a behaviour was reported [24].

Many different models with n = 2 have been developed to explain this behaviour based on different relaxation processes of the stresses generated by the sliding of the grains: dislocation motion inside the grains or along the grain boundaries, diffusional flow, interface-reaction-controlled diffusion, grain boundary migration, etc. [32]. Although none of them is able to explain successfully the body of experimental data in superplastic materials, they predict that diffusion either in the grain interior or along grain boundaries is the rate-limiting step for creep. From the analysis of a large variety of polycrystalline metallic materials with n = 2, Sherby et al. [32] derived two phenomenological relationships for grain boundary and lattice diffusion-controlled grain boundary sliding:

$$\dot{\varepsilon} = 2\text{x}10^{5}\,\frac{Gb}{k_B T}\left(\frac{b}{d}\right)^{3}\left(\frac{\sigma}{G}\right)^{2} D^{gb} \qquad (2a)$$

$$\dot{\varepsilon} = 8\text{x}10^{6}\,\frac{Gb}{k_B T}\left(\frac{b}{d}\right)^{2}\left(\frac{\sigma}{G}\right)^{2} D^{lat} \qquad (2b)$$

where b is the Burgers vector, G is the shear modulus and D^{lat} and D^{gb} are the effective diffusion coefficients for lattice and grain boundary diffusion, respectively. The first equation has been shown to account for the creep behavior of fine-grained oxyapatite [30] and $YBa_2Cu_3O_{7-x}$ superconductor [33]; the second equation reproduces adequately the experimental data of 3YTZP [25]. For this material, Swaroop et al. [31] have shown that an interface-controlled diffusion creep model developed by Schneibel and Hazzledine [34] expressed as:

$$\dot{\varepsilon} = \frac{33G}{k_B T}\left(\frac{b}{d}\right)^{2}\left(\frac{\sigma}{G}\right)^{2} \delta D^{gb} \qquad (3)$$

(with δ the grain boundary thickness) could also rationalized the experimental creep data. Such a model has not been used in this study because the grain boundary diffusivity D^{gb} derived from Eq. (3) for the present material is within a factor of 2 to that obtained from Eq. (2a).

In compounds, the diffusion coefficients D^{lat} and D^{gb} in the previous equations are an effective "molecular" diffusion coefficient, which takes into account the transport of the various ionic species, and usually reduces to that of the slower moving species [31]. In yttrium-doped barium zirconate, oxygen diffuses much faster than cations, with a bulk activation energy of 115 kJ/mol [35]. The creep activation energy of 570 kJ/mol measured in this work can be thus associated with the diffusion energy of cations in 15 at% yttrium-doped barium zirconate. Sakinas et al. [36] have recently determined the tracer diffusion coefficients of Zr^{4+} and Ba^{2+} cations in polycrystalline, undoped $BaZrO_3$ (97% relative density, d = 1.1 μm), both in bulk and along grain boundaries. They found that Ba^{2+} diffuses much faster than Zr^{4+}, regardless the diffusion path, and that the diffusion of both cations along grain boundaries is four orders of magnitude higher than lattice diffusion. The corresponding activation energies were 300 - 360 and 400 - 440 kJ/mol for grain boundary and lattice diffusion, respectively. These experimental diffusivities are shown in **Fig. 14**, along with the effective cation diffusivities deduced from the deformation experiments assuming either grain boundary D^{gb} (Eq. 2a) or lattice D^{lat} (Eq. 2b) diffusion-controlled creep; a Burger vector b = 3 Å and shear modulus G = 70 GPa [37] have been used in the calculations. It can be seen that the cation diffusivities measured in the diffusion experiments are two orders of magnitude higher than the effective values derived from creep tests, regardless the diffusion path; the corresponding diffusion energies are also smaller than the value of 570 kJ/mol found in this study.

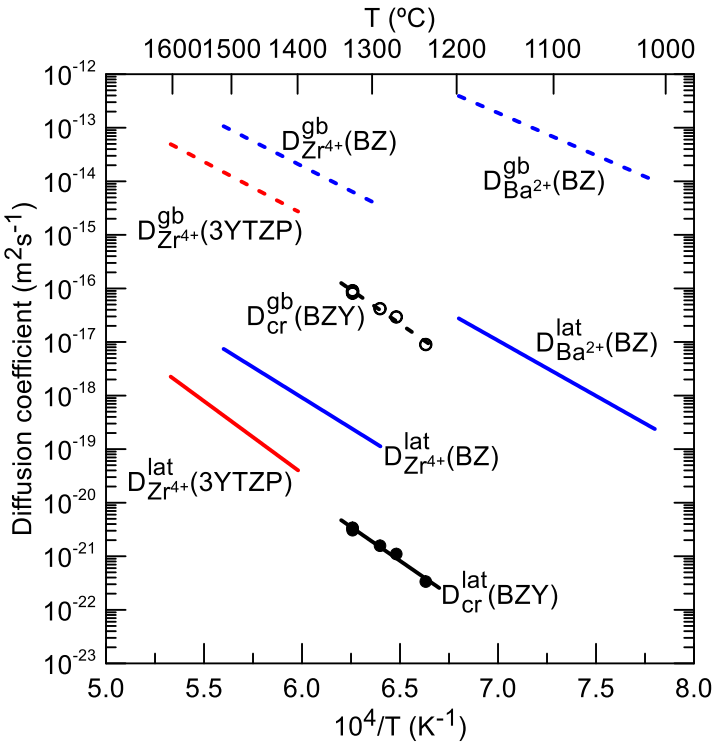

Fig. 14. Effective diffusion coefficients D_{cr}^{lat} and D_{cr}^{gb} for fine-grained 15 at% yttrium-doped barium zirconate (BZY) deduced from deformation data by using Eqs. 2a and 2b (in black). Cation tracer diffusion coefficients of Zr^{4+} and Ba^{2+} in undoped $BaZrO_3$ (BZ) [36] are also included (in blue). Tracer diffusion coefficients of Zr^{4+} (the creep rate-limiting species) in 3YTZP [31] (in red) are also shown for comparison. (lat = lattice diffusion, gb = grain boundary diffusion).

The differences in diffusivities deduced from the diffusion and creep studies can be rationalized, at least qualitatively, by considering the effect of yttrium doping on the self-diffusivities of the host cations, since the diffusion experiments were performed in undoped barium zirconate, whereas the creep tests have been carried out on a 15 at% yttrium-doped material. Due to the lack of diffusion data on doped barium zirconate, a comparison with other ceramic oxides seems to be pertinent in this context.

In yttria-stabilized zirconia, the most studied ceramic oxide during the last three decades, oxygen diffuses much faster than cations in both lattice and grain boundaries, the creep rate being thus cation-diffusion controlled [25], as in the present material. Experimental and theoretical studies have shown that yttrium segregates to grain boundaries [38-41] with an enrichment factor that increases with decreasing dopant content, being maximal for tetragonal zirconia (stabilized with < 4 mol% yttria) and minimal for cubic zirconia (stabilized with > 8 mol% yttria). Such an yttrium segregation has been related with the rather sluggish grain growth found in tetragonal zirconia compared with cubic zirconia [25, 31]], which may reflect a decrease in the diffusivities of the slower moving species (zirconium cations). Similarly, it has been reported that yttrium and zirconium segregate to grain boundaries in doped alumina, strongly decreasing the creep rates even down to more than two orders of magnitude with respect to the pristine material [27, 42, 43]; this feature was again correlated with a decrease in diffusivity of the rate-controlling species for creep.

In the present material, both numerical and experimental studies have also reported the segregation of yttrium cations at grain boundaries [44-47], as found in zirconia and alumina. It is therefore plausible that the kinetics of cation transport in yttrium-doped barium zirconate is slower than in the undoped material, explaining the differences in diffusivities. This suggestion is also supported by two additional features:

(i) Comparison of the absolute values of the creep rates in the present material and in fine-grained 3YTZP (**Fig. 9**) shows that zirconia is the softer material, even if the difference in grain size (d = 0.5 µm for 3YTZP, d = 0.2 µm for BZY) has not been considered in such a comparison; the difference increases in a factor between 6 and 15 depending on value of the grain size exponent p in Eqs. 2 and 3). Because both materials have a similar shear modulus G (70 GPa for BZY [37], 58 GPa for zirconia [31]) and Burger vector (~ 3 Å for BZY and zirconia), Eqs. 2 and 3 imply that the diffusivity of the rate-controlling species in BZY must be lower than in 3YTZP, as experimentally found on the contrary, the use of the diffusivities for undoped barium zirconate in Eqs. (2) and (3) would result in a BZY material softer than zirconia.

(ii) Along with creep, other mass transport-controlled processes such as sintering, densification and grain growth, are intimately related to the diffusion of the slowest moving species. It has been shown that the sintering of yttrium-doped barium zirconate is more demanding than in the undoped material, resulting in lower grain sizes and densities for similar experimental conditions [36, 48-50], suggesting again that yttrium-doping decreases the diffusivity of zirconium cations.

Regarding the activation energy for creep Q = 570 kJ/mol = 5.9 eV found in this work, it is not possible to elucidate directly from the deformation data whether it corresponds to volume or grain boundary diffusion. In the above-mentioned studies on creep in doped zirconia and alumina, activation energies higher than in the undoped materials were systematically reported, which correlates with the increase in Q found in this work with respect to undoped barium zirconate. Moreover, creep studies in perovskite-structured oxides, though scarce, have reported activation energies between 490 and 750 kJ/mol (490 kJ/mol in $BaCe_{0.95}Y_{0.05}O_3$ and $BaCe_{0.95}Yb_{0.05}O_3$ [29, 51], 630 kJ/mol in $SrTiO_3$ [52], 490 kJ/mol in $La_{0.9}Sr_{0.1}MnO_3$ [53], 520 kJ/mol in $La_{0.8}Sr_{0.2}Ga_{0.85}Mg_{0.15}O_3$ [54], 470 kJ/mol in $SrCo_{0.8}Fe_{0.2}O_3$ [55], 750 kJ/mol in $CaTiO_3$ [56] and 720 kJ/mol in $BaTiO_3$ [57]), which were associated with cation lattice diffusion. The present Q value compares adequately with these energies, suggesting that cation lattice diffusion is also the rate-limiting mechanism. The determination of the grain size exponent p, usually with p = 3 for grain boundary diffusion (Eq. 2a) and p = 2 for lattice diffusion (Eq.2b), would help to determine the diffusion path. However, the excellent microstructural stability against temperature exhibited by the material prevented different grain sizes from being obtained. For instance, Shirpour et al. [45] reported the absence of grain growth in BZY after annealing at 1700 °C for 24 h; also, the creep curves showed in **Fig. 12** and **Fig. 13** lasted more than one week, without modifications in grain parameters. New studies are therefore necessary to characterize the diffusion properties of acceptor-doped barium zirconates.

4 Conclusion

High dense and very fine-grained 15 at% yttrium-doped barium zirconate (BZY) polycrystals have been fabricated by a conventional sintering route starting from nanopowders synthesized by a modified EDTA - citrate complexing method. XRD analyses detected the presence of the single $Pm\bar{3}m$ perovskite phase in both the nanopowders and the sintered material. The microstructure is formed by fine and equiaxed grains with an average size of 0.20 μm. Mechanical tests have been performed at constant strain rate and at constant load in compression at temperatures between 1100 and 1325 °C (0.46 - 0.58 homologous temperature) in air. A transition brittle-to-ductile has been found with increasing temperature and/or decreasing strain rate. Extended steady states of deformation were attained in the ductile region, characterized by a stress exponent n

of 2 and an activation energy Q of 570 kJ/mol. The value of n, along with the absence of creep transients and modifications in grain shape after testing, suggests that grain boundary sliding is the primary deformation mechanism. The effective diffusivities deduced from mechanical data are about two orders of magnitude lower than the cation diffusivities measured in undoped barium zirconate. The difference is suggested to be due to yttrium segregation at grain boundaries, as found in yttrium-doped alumina and zirconia ceramics, which confers to the material an excellent microstructural stability and creep resistance at high temperatures. Based on deformation data for other perovskite oxides, it is more likely that volume diffusion would be the creep rate-limiting step.

5 Acknowledgment

This work was supported by the University Paris-Saclay (IDEX 2014), the Centre National de la Recherche Scientifique (Program "Instrumentation aux limites"), the University of Sevilla (VI PPIT-US) and the Spanish Ministerio de Ciencia, Innovación y Universidades (MAT2016-76526-R).

6 References

1. Shimada, T., et al., *The high temperature proton conductor BaZr0.4Ce0.4In0.2O3−α.* Journal of Power Sources, 2004. **131**(1): p. 289-292.
2. Costa, R., et al., *Tape casting of proton conducting ceramic material.* Journal of Applied Electrochemistry, 2009. **39**: p. 485-495.
3. Kreuer, K.-D., *Proton-conducting oxides.* Annual Review of Materials Research, 2003. **33**(1): p. 333-359.
4. Kreuer, K.D., *On the development of proton conducting materials for technological applications.* Solid State Ionics, 1997. **97**(1): p. 1-15.
5. Cerri, I., et al., *Scientific Assessment in support of the Materials Roadmap enabling Low Carbon Energy Technologies.* European Commission Joint Research Centre Institute for Energy and Transport, Petten, 2012.
6. Singhal, S.C., *Solid oxide fuel cells for stationary, mobile, and military applications.* Solid State Ionics, 2002. **152**: p. 405-410.
7. Steele, B.C.H. and A. Heinzel, *Materials for fuel-cell technologies.* Nature, 2001. **414**(6861): p. 345-352.
8. Bouhala, L., et al., *Study of interface influence on crack growth: Application to Solid Oxide Fuel Cell like materials design.* Materials & Design, 2010. **31**(3): p. 1033-1041.
9. Biswas, S., et al., *High-temperature mechanical properties of reduced NiO–8YSZ anode-supported bi-layer SOFC structures in ambient air and reducing environments.* Ceramics International, 2013. **39**(3): p. 3103-3111.
10. Selçuk, A. and A. Atkinson, *Elastic properties of ceramic oxides used in solid oxide fuel cells (SOFC).* Journal of the European Ceramic Society, 1997. **17**(12): p. 1523-1532.
11. Young, J.L. and V.I. Birss, *Crack severity in relation to non-homogeneous Ni oxidation in anode-supported solid oxide fuel cells.* Journal of Power Sources, 2011. **196**(17): p. 7126-7135.
12. Ryu, K.H. and S.M. Haile, *Chemical stability and proton conductivity of doped BaCeO3–*

BaZrO3 solid solutions. Solid State Ionics, 1999. **125**(1–4): p. 355-367.
13. Akbarzadeh, A.R., et al., *Combined theoretical and experimental study of the low-temperature properties of ${\mathrm{BaZrO}}_{3}$.* Physical Review B, 2005. **72**(20): p. 205104.
14. Babilo, P., T. Uda, and S.M. Haile, *Processing of yttrium-doped barium zirconate for high proton conductivity.* Journal of Materials Research, 2007. **22**(5): p. 1322-1330.
15. Yamazaki, Y., R. Hernandez-Sanchez, and S.M. Haile, *High Total Proton Conductivity in Large-Grained Yttrium-Doped Barium Zirconate.* Chemistry of Materials, 2009. **21**(13): p. 2755-2762.
16. Tong, J., et al., *Solid-state reactive sintering mechanism for large-grained yttrium-doped barium zirconate proton conducting ceramics.* Journal of Materials Chemistry, 2010. **20**(30): p. 6333-6341.
17. Pergolesi, D., et al., *High proton conduction in grain-boundary-free yttrium-doped barium zirconate films grown by pulsed laser deposition.* Nat Mater, 2010. **9**(10): p. 846-852.
18. Zhu, B., X. Liu, and T. Schober, *Novel hybrid conductors based on doped ceria and BCY20 for ITSOFC applications.* Electrochemistry Communications, 2004. **6**(4): p. 378-383.
19. Iakovleva, A., *Study of novel proton conductors for high temperature Solid Oxide Cells*. 2015, Université Paris-Saclay.
20. Poirier, J.-P., *Creep of Crystals: High-Temperature Deformation Processes in Metals, Ceramics and Minerals*. Cambridge Earth Science Series. 1985, Cambridge: Cambridge University Press.
21. Iguchi, F., et al., *The relationship between chemical composition distributions and specific grain boundary conductivity in Y-doped BaZrO3 proton conductors.* Solid State Ionics, 2009. **180**(6–8): p. 563-568.
22. Duval, S., *Y-Substituted Barium Zirconate, a Proton Conducting Electrolyte for Applications at Intermediate Temperatures* Thesis 2008, University of Munich.
23. Magrez, A. and T. Schober, *Preparation, sintering, and water incorporation of proton conducting Ba 0.99 Zr 0.8 Y 0.2 O 3− δ: comparison between three different synthesis techniques.* Solid State Ionics, 2004. **175**(1): p. 585-588.
24. WAKAI, F., S. SAKAGUCHI, and Y. MATSUNO, *Superplasticity of yttria-stabilized tetragonal ZrO 2 polycrystals.* Advanced Ceramic Materials, 1986. **1**(3): p. 259-263.
25. Jiménez-Melendo, M., A. Domínguez-Rodríguez, and A. Bravo-León, *Superplastic Flow of Fine-Grained Yttria-Stabilized Zirconia Polycrystals: Constitutive Equation and Deformation Mechanisms.* Journal of the American Ceramic Society, 1998. **81**(11): p. 2761-2776.
26. Wakai, F. and H. Kato, *Superplasticity of TZP/Al 2 0 3 Composite.* Adv. Ceram. Mat, 1988. **3**(1): p. 71-76.
27. Wakai, F., T. Nagano, and T. Iga, *Hardening in Creep of Alumina by Zirconium Segregation at the Grain Boundary.* Journal of the American Ceramic Society, 1997. **80**(9): p. 2361-2366.
28. Chen, T., F.A. Mohamed, and M.L. Mecartney, *Threshold stress superplastic behavior and dislocation activity in a three-phase alumina–zirconia–mullite composite.* Acta Materialia, 2006. **54**(17): p. 4415-4426.
29. Vaquero-Aguilar, C., et al., *High-temperature mechanical behavior of polycrystalline yttrium-doped barium cerate perovskite.* Journal of the European Ceramic Society, 2011. **31**(7): p. 1333-1338.
30. Ciria, D., et al., *Creep properties of high dense La9.33Si6O26 electrolyte for SOFCs.* Journal of the European Ceramic Society, 2020.
31. Swaroop, S., et al., *Lattice and grain boundary diffusion of cations in 3YTZ analyzed using SIMS.* Acta Materialia, 2005. **53**(19): p. 4975-4985.
32. Nieh, T.G., et al. *Superplasticity in Metals and Ceramics*. 1997.

33. Jiménez-Melendo, M., A. Domínguez-Rodríguez, and J.L. Routbort, *Deformation maps of YBa2Cu3O7 – x superconductors.* Scripta Metallurgica et Materialia, 1995. **32**(4): p. 621-626.
34. Schneibel, J. and P. Hazzledine, *The role of Coble creep and interface control in superplastic Sn-Pb alloys.* Journal of materials science, 1983. **18**(2): p. 562-570.
35. Farlenkov, A.S., et al., *Oxygen isotope exchange in doped calcium and barium zirconates.* Solid State Ionics, 2016. **290**: p. 108-115.
36. Sažinas, R., et al., *Tracer diffusion of 96Zr and 134Ba in polycrystalline BaZrO3.* Physical Chemistry Chemical Physics, 2017. **19**(32): p. 21878-21886.
37. Ciria, D., *Thermomechanical properties of materials for fuel cells, Tesis*. 2017, Univesity Paris-Saclay and University of Sevilla.
38. Theunissen, G.S.A.M., A.J.A. Winnubst, and A.J. Burggraaf, *Surface and grain boundary analysis of doped zirconia ceramics studied by AES and XPS.* Journal of Materials Science, 1992. **27**(18): p. 5057-5066.
39. Hines, J.A., et al., *The influence of trace impurities on the mechanical characteristics of a superplastic 2mol% yttria stabilized zirconia.* Acta Materialia, 1998. **46**(15): p. 5557-5568.
40. Matsui, K., H. Yoshida, and Y. Ikuhara, *Grain-boundary structure and microstructure development mechanism in 2–8mol% yttria-stabilized zirconia polycrystals.* Acta Materialia, 2008. **56**(6): p. 1315-1325.
41. Zhang, L. and A.V. Virkar, *On Space Charge and Spatial Distribution of Defects in Yttria-Stabilized Zirconia.* Journal of the Electrochemical Society, 2017. **164**(13): p. F1506-F1523.
42. Yoshida, H., et al., *Improvement of high-temperature creep resistance in fine-grained Al2O3 by Zr4+ segregation in grain boundaries.* Philosophical Magazine Letters, 1997. **76**(1): p. 9-14.
43. Yasuda, S., et al., *Improvement of High-temperature Creep Resistance in Polycrystalline Al₂O₃ by Cations Co-doping.* MATERIALS TRANSACTIONS, 2004. **45**(7): p. 2078-2082.
44. Iguchi, F., N. Sata, and H. Yugami, *Proton transport properties at the grain boundary of barium zirconate based proton conductors for intermediate temperature operating SOFC.* Journal of Materials Chemistry, 2010. **20**(30): p. 6265-6270.
45. Shirpour, M., et al., *Dopant Segregation and Space Charge Effects in Proton-Conducting BaZrO3 Perovskites.* The Journal of Physical Chemistry C, 2012. **116**(3): p. 2453-2461.
46. Helgee, E.E., A. Lindman, and G. Wahnström, *Origin of Space Charge in Grain Boundaries of Proton-Conducting BaZrO3.* Fuel Cells, 2013. **13**(1): p. 19-28.
47. Uthayakumar, A., A. Pandiyan, and S.B. Krishna Moorthy, *Yttrium dependent space charge effect on modulating the conductivity of barium zirconate electrolyte for solid oxide fuel cell.* International Journal of Hydrogen Energy, 2018. **43**(52): p. 23488-23499.
48. Sin, A., et al., *Synthesis and Sintering of Large Batches of Barium Zirconate Nanopowders.* Journal of the American Ceramic Society, 2002. **85**(8): p. 1928-1932.
49. Talib, I.A., M. Laidoudi, and R. Omar, *Study of Proton Conduction in Yttrium-Doped BaZrO 3 at High Temperature*, in *Solid State Ionics: Materials and Devices*. 2000, World Scientific. p. 559-564.
50. Babilo, P. and S.M. Haile, *Enhanced Sintering of Yttrium-Doped Barium Zirconate by Addition of ZnO.* Journal of the American Ceramic Society, 2005. **88**(9): p. 2362-2368.
51. Vaquero-Aguilar, C. and M. Jiménez-Melendo, *Characterization and creep properties of proton-conducting Yb-doped barium cerate.* Journal of the European Ceramic Society, 2011. **31**(14): p. 2671-2676.
52. Singh, D., et al., *High-temperature deformation behavior in SrTiO3 ceramics.* Journal of the European Ceramic Society, 2007. **27**(11): p. 3377-3384.
53. Wolfenstine, J., et al., *Elevated temperature deformation of fine-grained La{sub 0.9}Sr{sub*

0.1}MnO{sub 3}. Journal of Materials Research, 1996: p. Medium: X; Size: pp. 657-662.
54. Wolfenstine, J., P. Huang, and A. Petric, *Creep behavior of doped lanthanum gallate versus cubic zirconia.* Solid State Ionics, 1999. **118**(3): p. 257-259.
55. Majkic, G., L. Wheeler, and K. Salama, *Creep of polycrystalline SrCo0.8Fe0.2O3−δ.* Acta Materialia, 2000. **48**(8): p. 1907-1917.
56. Li, P., S.-i. Karato, and Z. Wang, *High-temperature creep in fine-grained polycrystalline CaTiO 3, an analogue material of (Mg, Fe)SiO 3 perovskite.* Physics of the Earth and Planetary Interiors, 1996. **95**(1): p. 19-36.
57. Park, E.T., et al., *High-temperature creep of polycrystalline BaTiO3.* Journal of Materials Research, 2011. **14**(2): p. 523-528.